

# High Sensitivity of Non-Fullerene Organic Solar Cells Morphology and Performance to a Processing Additive

Obaid Alqahtani, Jie Lv, Tongle Xu, Victor Murcia, Thomas Ferron, Terry McAfee, Devin Grabner, Tainan Duan, and Brian A. Collins\*

Although solvent additives are used to optimize device performance in many novel non-fullerene acceptor (NFA) organic solar cells (OSCs), the effect of processing additives on OSC structures and functionalities can be difficult to predict. Here, two polymer-NFA OSCs with highly sensitive device performance and morphology to the most prevalent solvent additive chloronaphthalene (CN) are presented. Devices with 1% CN additive are found to nearly double device efficiencies to 10%. However, additive concentrations even slightly above optimum significantly hinder device performance due to formation of undesirable morphologies. A comprehensive analysis of device nanostructure shows that CN is critical to increasing crystallinity and optimizing phase separation up to the optimal concentration for suppressing charge recombination and maximizing performance. Here, domain purity and crystallinity are highly correlated with photocurrent and fill factors. However, this effect is in competition with uncontrolled crystallization of NFAs that occur at CN concentrations slightly above optimal. This study highlights how slight variations of solvent additives can impart detrimental effects to morphology and device performance of NFA OSCs. Therefore, successful scale-up processing of NFA-based OSCs will require extreme formulation control, a tuned NFA structure that resists runaway crystallization, or alternative methods such as additive-free fabrication.

O. Algahtani, V. Murcia, B. A. Collins Materials Science and Engineering Program Washington State University Pullman, WA 99164, USA E-mail: brian.collins@wsu.edu O. Alqahtani Department of Physics Prince Sattam bin Abdulaziz University Alkharj 11942, Saudi Arabia J. Lv, T. Xu, T. Duan Chongqing Institute of Green and Intelligent Technology Chinese Academy of Sciences Chongqing 400714, China T. Ferron, T. McAfee, D. Grabner, B. A. Collins Department of Physics and Astronomy Washington State University Pullman, WA 99164, USA T. McAfee Advanced Light Source Lawrence Berkeley National Laboratory Berkeley, CA 94720, USA

The ORCID identification number(s) for the author(s) of this article

can be found under https://doi.org/10.1002/smll.202202411.

DOI: 10.1002/smll.202202411

## 1. Introduction

Power conversion efficiency (PCE) in organic solar cells (OSCs) is rising now with a record surpassing 18%.[1,2] In solution-processed bulk heterojunction (BHJ) OSCs, non-fullerene acceptors (NFAs)such as Y6<sup>[3]</sup> and Y6-derivatives<sup>[2]</sup>—show higher performance than their fullerenebased counterparts.[4-6] In contrast to fullerenes, development in synthesis and designing for NFAs has allowed for achieving new molecules with more efficient visible to near infrared (NIR) absorption, faster electron mobility, and lower band gaps.<sup>[7,8]</sup> Chemical modification of NFAs and elemental substitution, such as halogenation, are strategies of molecular design to manipulate material properties.<sup>[9]</sup> For example, fluorination of electron-accepting molecules often tends to affect device performance by improving energy levels, suppressing recombination and increasing the electron withdrawal.[10] However, there have been relatively little investigation of the effects of different NFA halogen type on morphology.[11–13]

On the processing and fabrication side, methods like thermal annealing and solvent additives are commonly implemented to improve the morphology of BHJ active layers in OSCs.[14-18] Solvent additives have been found to not only better dissolve donor and acceptor materials but also increase film formation time to enhance the donor-acceptor phase separation.<sup>[15]</sup> However, the effectiveness and compatibility of solvent additives varies and depends on the solvent-solute materials.[14,15,19] In small-molecule:fullerene OSCs, in general, additives improve crystallinity which is considered as an additional factor that leads to phase separation. This favorably influences charge generation, recombination and extraction processes in many systems. [15,20-23] For example, 1,8-diiodooctane (DIO) and 1-chloronaphthalene (CN) are commonly used as plasticizing solvent additives to allow for phase separation and ordering in small-molecule OSCs.[24] By and large, there is a required balance between increasing phase separation to achieve an optimal length scale and domain composition/ordering for efficient exciton dissociation and oversized "strong" phase separation in small-molecule based OSCs. [15,23] The additive-sensitivity in device performance, in some small-molecule:fullerene cases, has been attributed to the additive amount controlling the www.advancedsciencenews.com www.small-journal.com

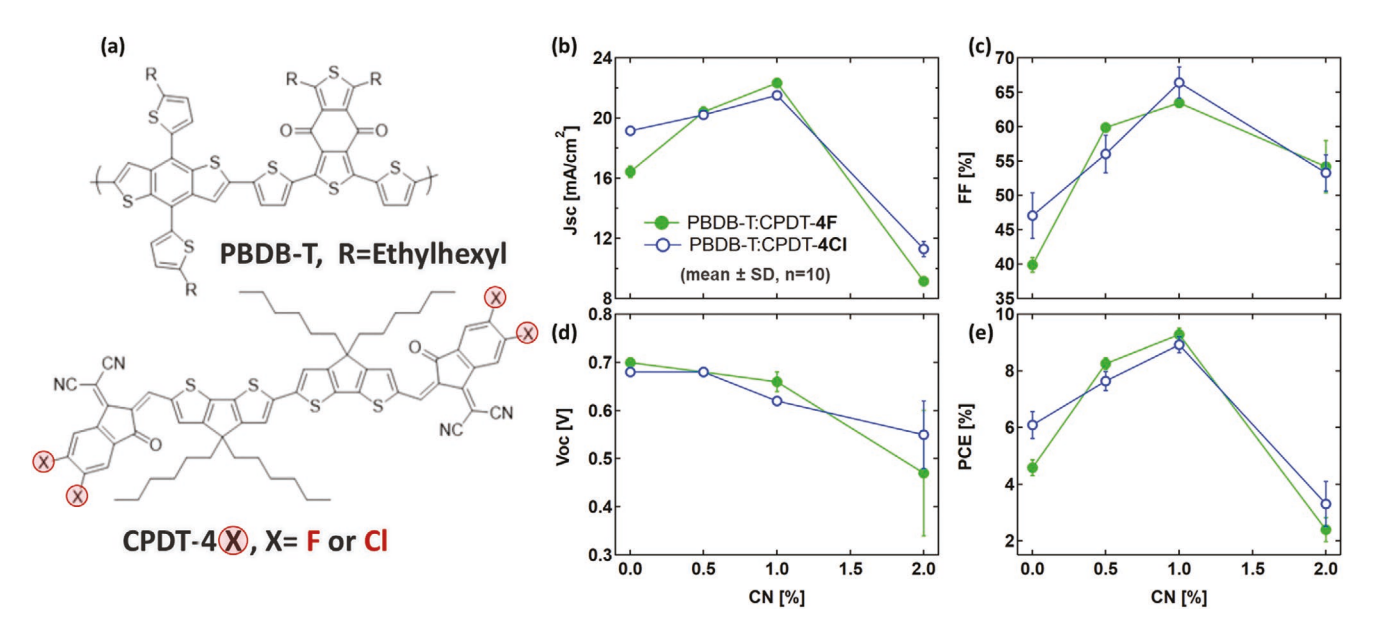


Figure 1. a) Chemical structures of the materials that were used to fabricate active layers in the investigated OSCs in this work. (Top) The polymer electron donor (PBDB-T) and (bottom) electron NFA acceptor (CPCD-4X, where X is Cl or F). The average parameters of device performance are plotted as a function of amounts of solvent additive (CN vol%); b) J<sub>sc</sub>, c) FF, d) V<sub>oc</sub>, and e) PCE at 1 sun. The solid green circles indicate the F-blends (PBDB-T:CPDT-4F) with (1:1) weight ratio and open blue circles represent the CI films (PBDB-T:CPDT-4CI) with (1:1.2) weight ratio. See Tables S1, S2 and Figure S1 (Supporting Information) for more about device performance, J-V curves, and external quantum efficiency (EQE) profiles. The device performance parameters are the mean of ten cells  $\pm$  standard deviation.

film morphology.<sup>[23]</sup> Polymer:fullerene OSCs generally are less sensitive to over crystallization or excessive phase separation. Despite the relative popularity, however, to our knowledge the strong phase separation effect occurring in high-performance polymer-NFA OSCs has not been studied in detail.

Recently, we have developed synthetically simple, NIR, CPDTbased NFAs for OSC applications (Figure 1a). [25] Those NFAs were paired in binary BHI OSCs with the electron-donating polymer—poly[[4,8-bis[5-(2-ethylhexyl)-2-thienyl]benzo[1,2-b:4,5b'|dithiophene-2,6-diyl|-2,5-thiophenediyl[5,7-bis(2-ethylhexyl)-4,8-dioxo-4H,8H-benzo[1,2-c:4,5-c']dithiophene-1,3-diyl]], (PBDB-T) (Figure 1a, top). The impacts of fluorination (F) and chlorination (Cl) of the NFA on the device performance were previously investigated revealing an extended absorption to the NIR region. Both NFAs show optical bandgap about 1.3 eV which is near ideal to achieve the maximum Shockley-Queisser limit, [26] and comparable to that of Y6 (1.33 eV). [3] Device performance noticeably was found to be very sensitive to the amount of additive where the efficiency almost doubles to about 10% at the optimal additive concentration. Beyond that, any extra amount, even 0.1%, of solvent additive results in drastic drops in device performance. The overall trends of device performance are comparable in OSCs with either F- or Cl-NFA variants.[25] The overall comparability in device performance of fluorinated versus chlorinated NFAs is common among many of the high-performing systems. For example, PM6:BTP-4F (Y6) and PM6:BTP-4Cl yield ≈16.5% PCE, PM7:TPIC-4F/4Cl give ≈15%, PM6:IT-4F/4Cl (≈13.4%),[11] and PBDB-T:FDICTF(2F)/ (2Cl) yield about 16.5% PCE.<sup>[9]</sup> However, that cannot be generalized because other chlorinated NFAs slightly outperform their fluorinated analogs, e.g., PBDB-T:IPIC-4F gives 10.7% while its chlorinated derivative yields 13.0% PCE.[12]

In this work, we present a case study of these two CPDTbased NFAs to investigate the morphological origins of extreme performance sensitivity to the CN processing additive. Many CPDT-based NFAs have been synthesized and investigated for OSC applications. [27-29] However, this is the first study to investigate the morphological evolution and sensitivity of this type of materials to the concentration of CN solvent additive. Findings of this work underscore the importance of continuing to explore scale-up processing strategies for industrialization of NFA OSCs. Our investigation of the F- and Cl-active layers reveals the high sensitivity of their performance and morphology to the concentration of the solvent additive. The morphological characterization indicates that domain purity and molecular packing are enhanced with the additive amount up to the optimal concentration of 1 vol%. Both morphological aspects, crystallinity and domain purity, are highly correlating with device fill factor (FF) and short-circuit current density ( $J_{sc}$ ) in the investigated systems. Thus, optimal concentration of CN (1%) almost doubled the device PCE compared to the BHJ devices without the additive. However, amounts of CN beyond the optimum concentration results in over-crystallization and strong phase separation as manifested in micrometer-scale pure NFA crystallites, as in the case of blends with 2% CN. As a result, the device performance is significantly hindered due to inefficient exciton dissociation and increased charge recombination. This result indicates that NFAs in general face a similar challenge to scale up as in comparison to their all small-molecule counterparts. Morphologies in F-blends versus Cl-blends are found to be similar except for a stronger tendency of Cl-based NFA to aggregate into crystallites, which may be due to enhanced interaction with the CN additive.





## 2. Results

#### 2.1. Device Performance

Figure 1b-e presents the device performance parameters of the investigated OSCs, processed from chlorobenzene (CB) with different CN additive concentrations. More performance details can be found in Figure S1 and Tables S1 and S2 (Supporting Information). The  $J_{\rm sc}$  increases with the additive up to 1% (vol%) CN, where maximum  $I_{sc}$  values are about 22 mA cm<sup>-2</sup> for both systems, then significantly drops down in the blends with 2% CN. The FF follows a similar trend as  $I_{sc}$  in both the F- and Cl-systems, with maximum FF values about 63% and 66%, respectively. On the other hand, the  $V_{\rm oc}$  steadily decreases with addition of solvent additive, with the highest  $V_{oc} \approx 0.7 \text{ V}$ for the blends without additives. At 1% CN,  $V_{\rm oc}$  drops to 0.66 and 0.62 V for the F- and Cl-systems, respectively. The lower  $V_{oc}$  relative to record systems such as PM6:Y6 likely originates from a less favorable energy level alignment. The performance of the devices as represented by PCE in Figure 1e follows closely the trends in the  $J_{\rm sc}$  and FF, with maximum PCE of 9.51% for the F-systems and 9.20% for the Cl-devices. Overall, the fluorinated and chlorinated cells exhibit similar device behaviors with the solvent additive (CN). The overall performance trends are very similar to those of our original work.<sup>[25]</sup> In that work, even an increment of 0.1% CN beyond the optimal concentration resulted in a considerable reduction (≈20%) in PCE.[25]

Previous measurements of  $I_{sc}$  and  $V_{oc}$  dependency on intensity of incident light suggest that both systems with 1% CN have bimolecular recombination that limits performance to some extent, which were attributed to unbalanced charge mobilities.<sup>[25]</sup> Overall, the Cl-blends show similar trends in device performance to the F-blends in this work and the previous work indicating good reproducibility. In the current work, the EQE spectra of the blends without and with 1% CN (Figure S1, Supporting Information) are similar to the published work in terms of their overall peak intensity, shape, and range, with the optimum devices having ≈70% EQE between ≈455 nm and the CPDT absorption edge at ≈850 nm. Generally, EQE follows the trends of device performance with solvent additive. However, the F-system exhibited higher trap-assisted recombination in the previous work, which was thought to originate from the morphology of active layer.[25]

# 2.2. Morphology: Grazing-Incidence Wide-Angle X-Ray Scattering

Now, we examine the morphological evolution of the active layers beginning with molecular ordering and packing via grazing-incidence wide-angle X-ray scattering (GIWAXS) measurements. [30] First, we examined pure films to determine how CN affects individual crystallization habits. The GIWAXS patterns of the PBDB-T donor polymer, presented in **Figure 2a**—c and Figure S2 (Supporting Information), show that the polymer has a face-on orientation with respect to the substrate surface. The solvent additive slightly enhances packing quality for both (100) and (010) by increasing the coherence length ( $D_{\rm coh}$ ) of both (Figure 4a,b, see red squares). Also, 1% of CN additive

increases the (010) face-on population which can be seen as an increase in the peak intensity (Figure 2c).

For pure NFA films, the scattering results (Figure 2 and the Supporting Information), show that both small molecules have  $\pi$ - $\pi$  stacking at  $q \approx 1.8 \text{ Å}^{-1}$  and lamellar at  $q \approx 0.33 \text{ Å}^{-1}$ corresponding to d-spacings of  $\approx$ 3.5 and 19 Å, respectively. For both small molecules,  $\pi$ – $\pi$  stacking populations are randomly oriented when processed without additive and orient mostly face-on to the substrate with 1% CN, as shown in the GIWAXS 2D images and pole figures in Figure 2. The OoP (010) peak intensity increases with the additive, suggesting an increase in the small molecule crystal population. Additionally, new packing structures appear in both small molecules with 1% CN—especially in CPDT-4F where a second face-on (010) population forms with a very narrow reflection at  $q \approx 1.7 \text{ Å}^{-1}$ (*d*-spacing of ≈3.7 Å, Figure 2e and Figure S3, Supporting Information). Due to the very different peak width, we interpret this to be a different polymorph as has been seen in other OSC small molecules.[31] The coherence length of the primary polymorph, on the other hand, does not improve with CN for  $\pi$ – $\pi$ stacking in both pure small molecules (blue and green squares in Figure 4a).

For the blends, the GIWAXS patterns are similar to the neat materials without any new formed packing structures (e.g., the second NFA polymorph) upon blending into BHJ films. The 1D scattering profiles are shown in Figure 3 (more data and analysis in the Supporting Information). The peak positions and d-spacing of lamellar and  $\pi$ - $\pi$  stacking are summarized in Table S3 (Supporting Information). The focus here is on the in plane (IP) scattering peaks of (100) "lamellar," and OoP (010) " $\pi$ - $\pi$ " stackings, because of their dominant effects on charge transport. In Figure 4a, surprisingly,  $D_{\rm coh}$  for  $\pi$ - $\pi$  stacking of both the NFA and polymer materials is constant within uncertainties and remains relatively short in all blends (≤4 nm) with no obvious trends with solvent additive. On the other hand,  $D_{coh}$ for lamellar of the polymer stacking increases with CN, in pure materials and blends, from 4 to 18 nm as shown in Figure 4b. D<sub>coh</sub> for lamellar of NFA stacking for in neat films with 1% CN was found to be  $\approx$ 40 nm. In blend films, Figure 4b,  $D_{\rm coh}$  of the NFAs monotonically increases with CN from 5 to 30 nm. Additionally, the intensities of both diffraction peaks (Figure 4c,d) of polymer and NFA materials in blends generally increase with CN. That suggests that rather than  $\pi$ – $\pi$  coherence, the crystal population is the main beneficiary of the additive in both F- and Cl-blends. The increase in lamellar coherence lengths, seen for all materials, suggests a straightening of the polymer backbone and alignment of NFAs leading to the increases  $\pi$ - $\pi$  stacking population. High crystalline domains are often considered beneficial in aiding charge transport.[32] Positive correlations between FF and molecular ordering of NFAs has been reported in many non-fullerene systems.[33]

#### 2.3. Morphology: Microscopy

**Figure 5** presents key results from a multimodal microscopy study of the Cl-blends. That includes using: carbon edge scanning transmission X-ray microscopy (STXM), transmission electron microscopy (TEM), atomic force microscopy (AFM),

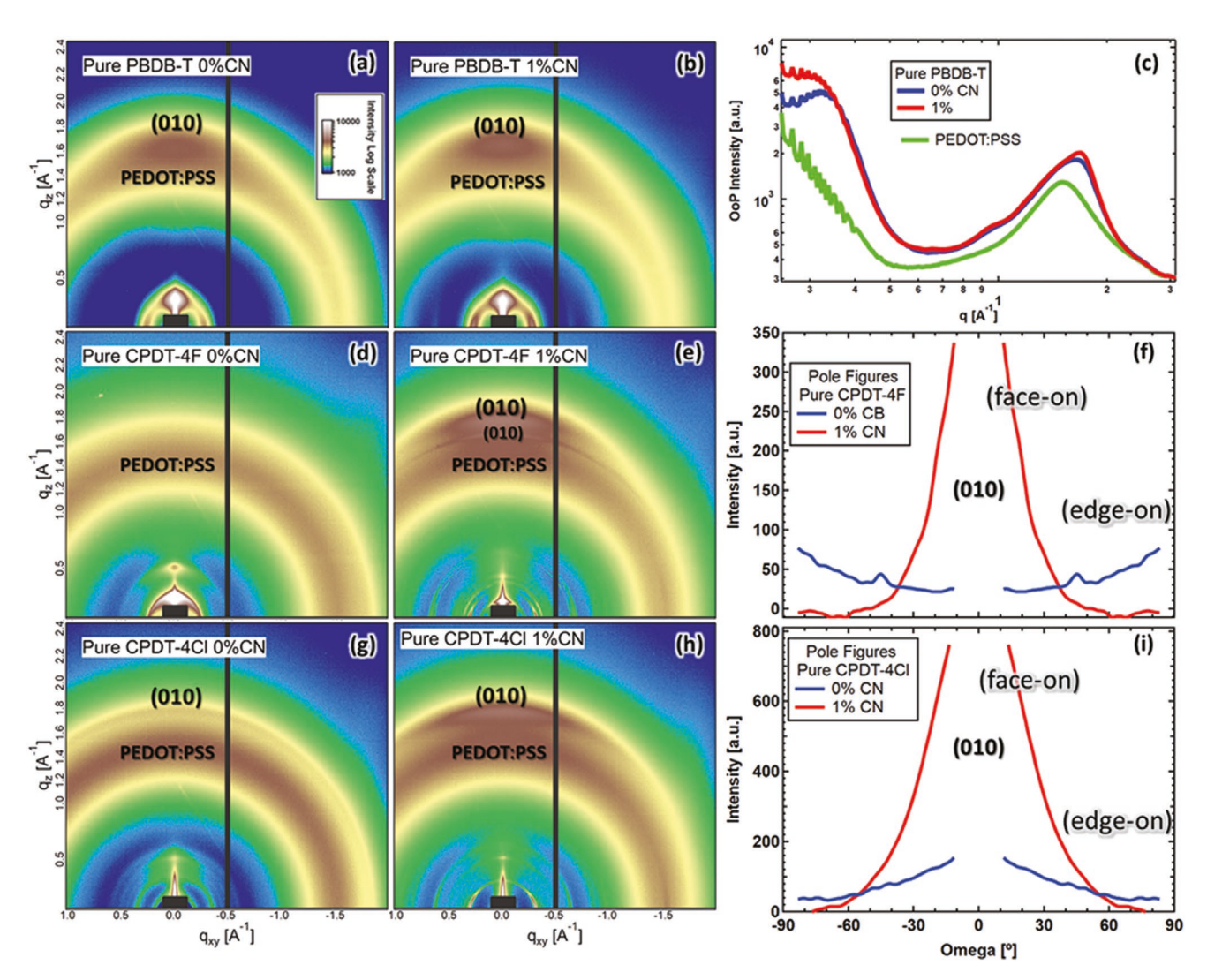


**Figure 2.** a,b,d,e,g,h) 2D GIWAXS images in as arbitrary color scale: pure materials without additive (left) and with 1% CN (middle). c) 1D GIWAXS profiles for pure polymer with and without CN extracted in the out of plane (OoP) direction to show changes in peak intensity of OoP  $\pi$ – $\pi$  stacking. The PEDOT:PSS background is appended to the graph in green for reference. f,i) Pole figures of  $\pi$ – $\pi$  stacking in pure CPDT-4F and pure CPDT-4Cl, respectively, without additive (blue) and with 1% CN (red).

(cross-sectional) scanning electron microscopy (SEM), and optical microscopy. STXM (Figure 5a,b; Figures S11 and S13, Supporting Information) and TEM (Figure 5d,e; Figures S26 and S27, Supporting Information) show that domains gradually coarsen and purify with the additive up to 1% CN, more noticeable in the Cl-blends. AFM scans (Figure 5g,h and Figures S20 and S21, Supporting Information) support and complement the STXM findings by showing that the film roughness increases with the concentration of solvent additive. The micrometerscale crystallization of Cl-NFA in the 1% CN blend film as measured by AFM is at odds with TEM and STXM because AFM was conducted on separate films. This sample-to-sample discrepancy shows just how sensitive the Cl-NFA is to the precise concentration of the additive. Notably, the F-blends were consistent across all measurements, possibly suggesting slightly less sensitivity.

In the F- and Cl-blends with 2% CN, strong phase separation and drastic domain growth take place, with domain

size at the micron scale. The micrometer-size features are confirmed with STXM spectroscopic scans of pure films (Figure S8, Supporting Information) to be NFA domains, likely large crystals. The NFA domains in the 2% blends were easily observed under TEM, SEM of topology and crosssections (Figure 5k-l; Figures S24 and S25, Supporting Information), and even under the optical microscope (Figure 5) and Figure S23, Supporting Information). In addition to the SEM images, AFM scans indicate that the NFA crystals bulge out of the film. Within those large domains, neither TEM nor STXM were able to resolve obvious features or textures that originate from D/A domains (Figures S11, S26, and S27, Supporting Information). The polymer and NFA sensitivity to the processing additive in the blends are similar to the pure films. The pure polymer films remain smooth and uniform with no significant changes with CN (Figures S28, S10, and S22, Supporting Information). On the other hand, STXM and TEM scans of neat films of F- and Cl-small molecules show some

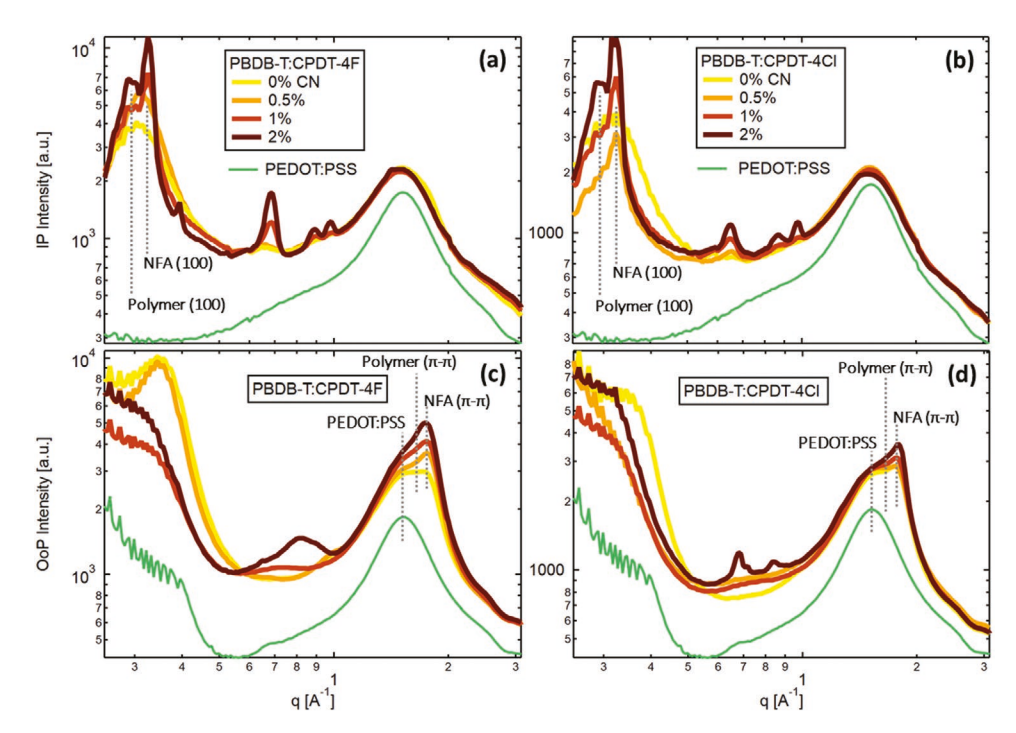
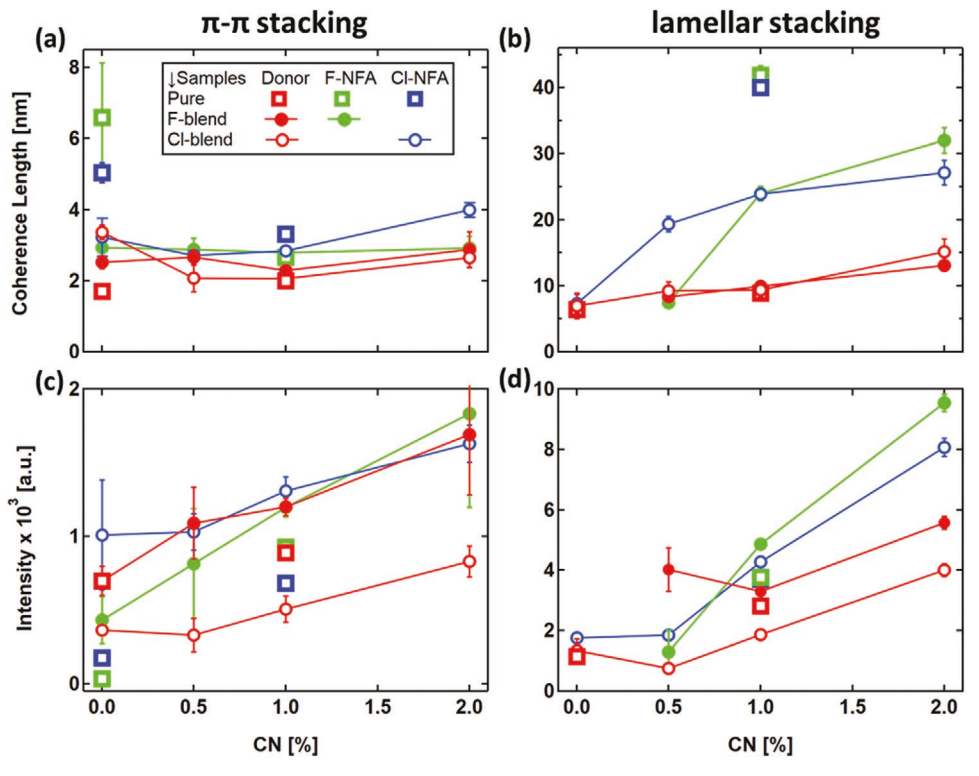


Figure 3. 1D GIWAXS profiles for all the investigated blends (as indicated in the legends)—plus PEDOT:PSS background shown in green. Profiles in the IP sector (top) and OoP (bottom). Data for a,c) PBDB-T:CPDT-4F blends and b,d) PBDB-T:CPCT-4Cl. More GIWAXS results and analysis can be found in the Supporting Information (Figures S2–S7 and Table S3, Supporting Information).



**Figure 4.** GIWAXS analysis of coherence length and peak intensity for neat films and blends as indicated in the legends. Diffraction coherence length versus CN vol% concentrations for a) out-of-plane  $\pi$ - $\pi$  stacking (010) and b) in-plane lamellar stacking (100). c,d) Analogous plots for diffraction peak intensity. The values are extracted from peaking fitting analysis of GIWAXS data, see examples and description in Figure S7 (Supporting Information).

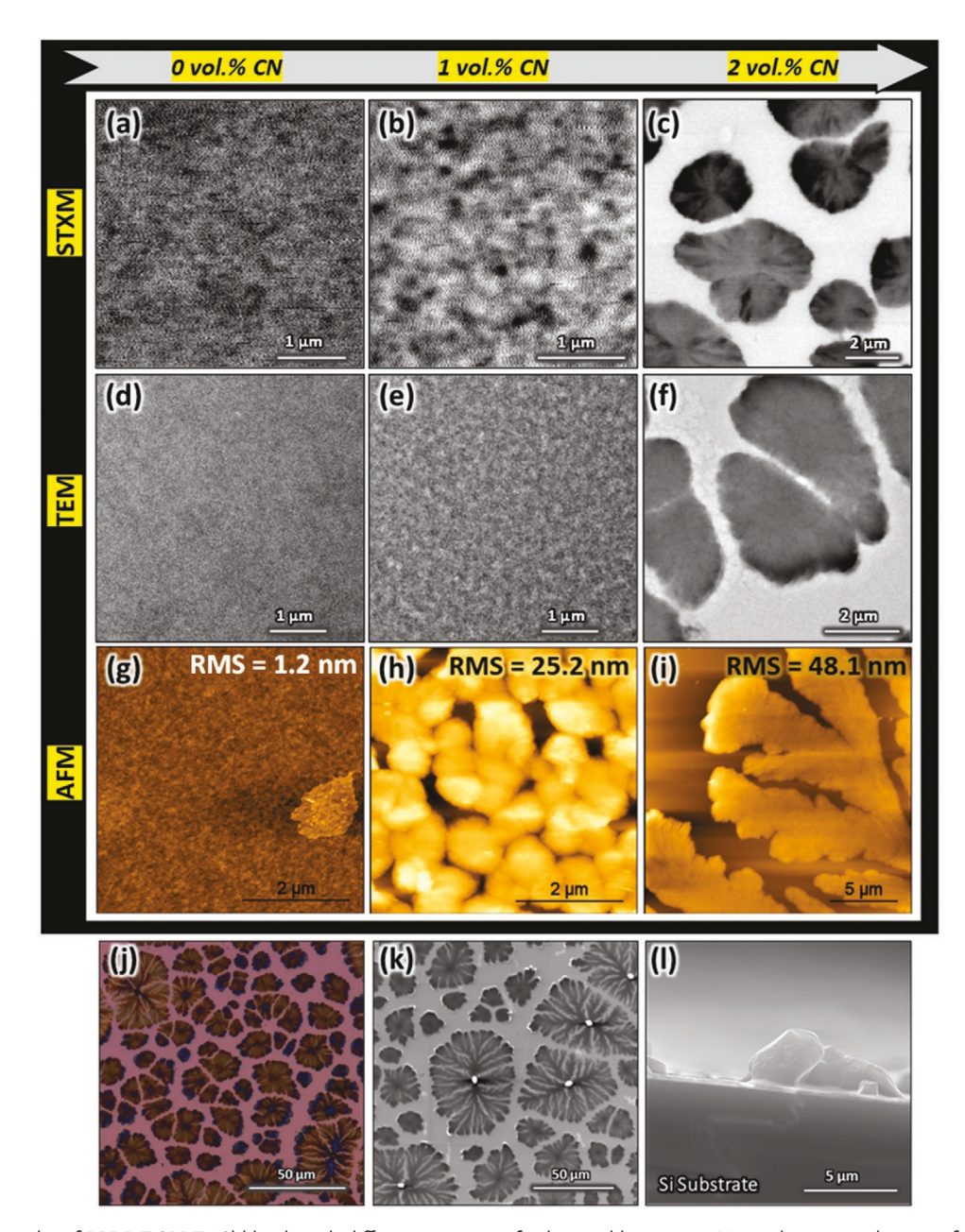


Figure 5. Micrographs of PBDB-T:CPDT-4Cl blends with different amounts of solvent additive using X-ray, electron, and atomic force microscopies. a–c) STXM scans for blend with 0%, 1%, and 2% CN, respectively, where dark regions represent NFA-rich domains (more in Figures S11–S15, Supporting Information). d–f) TEM scans of blend with 0%, 1%, and 2% CN, respectively (more in Figures S26 and S27, Supporting Information). g–i) AFM scans of blends with 0%, 1%, and 2% CN, respectively (more in Figures S20 and S21, Supporting Information). Scans of the Cl-blends with 2 vol% CN: j) an optical microscope scan (more in Figure S23, Supporting Information), k) a topology SEM scan, and l) cross-section SEM scan. More SEM scans in Figures S24 and S25 (Supporting Information). Scale bars are indicated for each scan.

textures that can be orientational domains or thickness variations (Figures S10 and S28, Supporting Information). Crystals of small molecules coarsen with CN—again more pronounced in the Cl-film than the F-film—leading to rougher film surfaces. TEM alone is not enough to conduct compositional analysis of the blends due to similarities in electron densities of the investigated NFA and polymer materials. STXM, on the other hand, is a more suitable tool to conduct this type of analysis because of its sensitivity of chemical bonds.

To quantitatively measure nanodomain composition in blends, we followed our previous methods of combining X-ray microscopy with spectroscopy. [34,35] Spatially averaged spectra of F- and Cl-blends—without and with 1% CN—confirm the average film composition, i.e., donor:acceptor weight ratios (Figure 6a, others in the Supporting Information). The results of composition mapping of the chlorinated blend with 1% CN, shown in Figure 6b, show that pure small-molecule and pure polymer domains exist in this blend, which is with

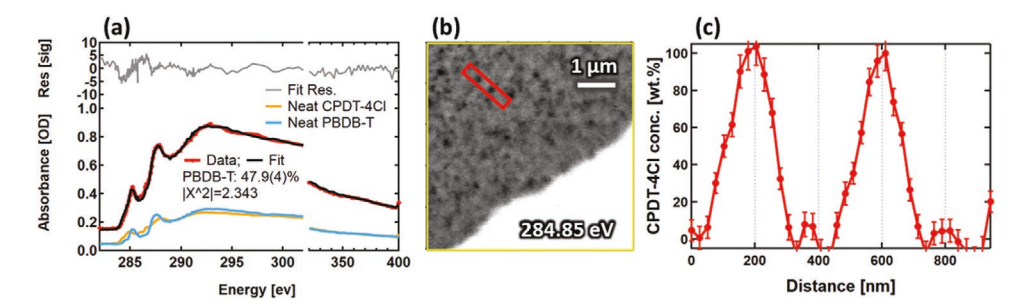


Figure 6. PBDB-T:CPDT-4Cl with 1 vol% CN blend. a) NEXAFS spectra for the blend and neat films (as indicated in the legends). The fit (black) of the NEXAFS spectrum of the blend (red) confirms the average weight ratio (i.e., ≈55% small molecule). b) A STXM image that was acquired at 284.85 eV, which is a small molecule resonant energy. The dark regions indicate small molecule domains, and the gray regions indicate polymer-rich domains. c) Compositional line out represents variation of the small molecule concentration across different domains along the red rectangle that is indicated on the STXM image in (b) (for more details, refer to Figure S14, Supporting Information).

optimal concentration of CN. The extracted composition profile (Figure 6c) reveals ≈200 nm NFA domains surrounded by polymer. Having pure domains in polymer-small molecule OSCs has been proven to be beneficial for device performance by reducing charge recombination, [36] but 200 nm domains may be too large for efficient exciton capture. Such quantitative compositional mapping was not viable for the F-blends up to 1% CN due to the domain size in those films being below the STXM resolution. [37,38] We attribute this to both the slightly higher NFA loading in Cl-blends (55% vs 50%) and the apparently increased propensity of the Cl-NFA to aggregate at lower CN concentrations than the F-NFA. The latter has been observed in blends (Figure 5h; Figures S20 and S21, Supporting Information) and pure films (Figures S22 and S28, Supporting Information).

For 2% CN blends (both F and Cl), the composition analysis (Figures S11-S15, Supporting Information) shows NFA-rich domains (≈65-70 wt%) surrounded by polymer-rich domains (≈60–90 wt% for Cl-blends, but pure for F-blends). Impure domains here are not at odds with the conclusion of pure NFA crystals because these compositional analyses average over the vertical direction of a film. Therefore, it is likely that a vertical stratification of pure domains takes place. If that is accurate, then the topology AFM and SEM scans of the 2% CN blends would suggest that NFA crystals form on top of the (NFA-depleted) film. In particular, the cross-sectional imaging shows that those large NFA crystals tower (tens of micrometers) over the film, which is taller than thicknesses of films in their wet stage of processing (wet films usually are a few microns thick). [31,39] We hypothesize that NFA runaway crystallization to be promoted by mobile NFA molecules that join from underneath then push large crystals upward with respect to the substrate surface. However, further work to understand what appears to be an interesting mechanism of film formation is required.

In short, both domain size and purity increase with solvent additive. Pure domains were detected in the Cl-blend with 1% CN, where domain purity is usually beneficial for device performance by reducing charge recombination. [36] Additional amount of additive beyond 1% CN results in strong phase separation leading to micron-scale NFA crystallites, which hinder exciton dissociation. The Cl-based films show increased sensitivity to the CN additive, aggregating and crystallizing at lower concentrations, even potentially being unstable to slight variations at the optimized concentration.

### 2.4. Morphology: Resonant Soft X-Ray Scattering

To further examine how domain size and purity evolve as the amount of CN increases, especially in the blends with domains that were not well-resolved by microscopy, we turn to resonant soft X-ray scattering (RSoXS).<sup>[40]</sup> In addition to domain size and purity, RSoXS as a technique is very helpful in gaining insights into phase volume fraction and molecular orientation.<sup>[32,41]</sup> Figure 7a,c shows the Lorentz corrected<sup>[42]</sup> scattering profiles for the F- and Cl-blends, respectively, versus the scattering vector (Q). For RSoXS, the donor–acceptor contrast is dependent on the index of refraction (Figure S8, Supporting Information). The Q-position of a scattering feature ( $Q^*$ ) approximately indicates the structure factor or spacing of scatterers called the characteristic length ( $Lc = 2\pi/Q^*$ ).<sup>[41]</sup>

For the F-blends, scattering data shown in Figure 7a show a feature that shifts to a lower Q with solvent additive, suggesting gradually growing domains with Lc increasing from about 30 to ≈60 nm. Data of the F-blend with 2% CN show that a secondary feature emerges at very low Q indicating morphological domains with size  $> 0.5 \mu m$ . We assign that to the NFA crystallites that were observed via microscopy. For all the Cl-blends, on the other hand, the scattering profiles show a primary feature ranging between Lc ≈ 25 and 50 nm with additive with a secondary feature appearing and shifting to lower Q with increasing CN. Like the F-system, the secondary peak in Cl-blend with 2% CN points toward formation of large NFA domains with sizes >0.5 µm (summarized in Figure S19, Supporting Information). For the Cl blend with 1 vol% CN, the secondary feature gives  $Lc \approx 200$  nm which is in good agreement with the STXM results (Figure 6c). Our results of examining anisotropic scattering patterns (Figures S16, S17, and S19, Supporting Information) show that there is no drastic change of molecular orientation with solvent additive or type of halogenation. Although orientational scattering might still present, we believe that is negligible compared to material scattering.

Thus far, the RSoXS results in agreement with STXM and GIWAXS in terms of domain-size growth with solvent additive. The scattering data also shows that multilength scale features appear with solvent additive, that happens sooner in the Cl-blends than the F-films. Multilength scale domains, often manifested as two peaks in the scattering profiles, have been observed in other binary and ternary BHJ blends. [43–45] Usually,

(b) 13 30 25 [a.u] [SI [a.u] 20 Intensity\*Q<sup>2</sup> 15 PBDB-T:CPDT-4F PBDB-T:CPDT-4 10 0% CN 0.5% (c) (d) PBDB-T:CPDT-4CI 0% CN 0.5% 60 0.9 Q\* Secondar 0.8 rsi [a.u] Intensity\*Q2 [a.u] O\* Primary 40 0.7 PBDB-T:CPDT-4CI 20

Figure 7. Scattering profiles and TSI for all blends. a) RSoXS 1D averaged profiles for PBDB-T:CPDT-4F blends. Their TSI and composition variation are shown in (b). TSI calculated by integrating areas under scattering profiles. Then the composition variation was calculated by normalizing TSI for all blends to TSI of the blend with 1% CN. c) 1D scattering profiles for the PBDB-T:CPDT-4Cl blends. d) TSI and composition variation values for the Cl-blends. In (b) and (d), the red circles represent TSI, and blue diamond shapes represent composition variation "average domain purity." This data were acquired at X-ray energy of 285.2 eV, Lorentz corrected, and corrected for X-ray fluorescence background, where X-ray energy of 285.2 eV is slightly below the resonant energy of the polymer material, to increase the material contrast. Additional scattering data taken at different energies can be found in Figures S16 and S17 (Supporting Information).

0%

0.5%

1%

CN [%]

3

Q [nm<sup>-1</sup>]

4 5 6 7 8

the scattering features at high Q are associated with a domain size that is crucial for device performance, that includes aspects such as exciton diffusion length and  $J_{\rm sc}$ . In this work, therefore, we refer to those high-Q scattering features as the primary features. To examine how average domain purity changes with solvent additive, the total "or integrated" scattering intensity (TSI) of the RSoXS profiles is commonly used. [32,36,41] Figure 7b.d presents the TSI, where the composition difference between domains (and therefore domain purity) is proportional to square root of TSI. That also can be used to investigate morphological details at the donor-acceptor interfaces. [37,46] The results show that the average domain purity in the examined blends increases with the amount of solvent additive up to 1% CN. Compared to the F-blends, the Cl-samples seem to purify faster with solvent additive. TSI results of the Cl-blends suggest that domain purity in the film with 0.5% CN is almost as high as in the 1% CN sample, where the latter consists of STXMmeasured pure domains.

The presence of multilength scale morphology, however, demands careful analysis of the RSoXS TSI to arrive to more reliable conclusions. The goal is to determine the significance of the component scattering intensity (CSI) of both the primary and secondary features. To examine that, we apply two-peak fitting and extracted the CSI values by following previous procedures that have been implemented to analyze multifeature RSoXS data of OSCs systems. [44,47] That analysis assumes multifeature scattering data comes from distinct uncorrelated structures. The multipeak fitting results and comparison (see

examples in Figure S18, Supporting Information) show that CSI of primary peaks is the main contributor to TSI, and the CSI of secondary features is negligible. Thus, we base our interpretations of domain purity being enhanced with CN on the observed increases in CSI of the primary peaks, which corresponds to morphological features with crucial size to performance. It is worth noting that TSI drops significantly for blends with 2% CN, which we attribute to reduction in phase volume fraction as many NFA molecules migrate into much larger domains.

Based on RSoXS and STXM results, the main finding is that domain purity in both halogenated systems increases with amount of solvent additive and reaches complete domain purity around 1 vol% CN. In general, domain purity has been viewed as a critical aspect of morphology that can be correlated to many device performance parameters in OSCs such as bimolecular recombination, FF, and  $J_{\rm Sc}$ .

#### 3. Discussion

Based on the combined morphological results, Figure 8 depicts the general trend of morphology evolution with CN additive in both halogenated systems. Red and blue colors represent NFA and polymer domains, respectively. The lines represent ordered NFA molecules (red) and ordered polymer chains (blue). With higher concentration of solvent additive, the length of the lines increases indicating improvement in the lamellar stacking, but

(010) π-π stacking

→ PBDB-T

→ NFA

∴ (100) lamellar

(LC)

O vol.% CN

1 vol.% CN

2 vol.% CN

characteristic length

**Figure 8.** A general depiction of morphology evolution with solvent additive (CN) in the investigated blends. Blue regions indicate polymer-rich domains with blue lines representing ordered polymer chains. The red regions represent NFA-rich domains with red lines indicating ordered molecules. The  $\pi$ - $\pi$  stacking of the polymer which is mostly face-on with respect to the substrate as depicted here does not mean that the direction of the fibril growth is known in those systems.

not in the  $\pi$ – $\pi$  stacking (refer to the coherence length results). It is noticeable as depicted that NFAs start with random crystal orientations (direction of the red lines) but prefer to orient face-on with respect to the substrate when CN is added. Additionally, the solvent additive increases populations of face-on  $\pi$ – $\pi$  stacking which was measured via GIWAXS as an increase in peak diffraction intensities of both NFA and polymer materials. For domain size, films processed from CB consist of small domains that slightly grow with solvent additive, in addition to large-scale domains that evolve with CN. Finally, domain purity increases with CN and is depicted as pure blue and pure red colors.

Since the F- and Cl-active layers show mostly similar trends in terms of their device performance with solvent additive (CN), they were expected to have similar morphologies. Our findings in general confirm that where solvent additive enhances domain purity, increases crystallinity and packing, and eventually leads to multilength scale domains in both systems. However, we find the main difference between the two systems is the higher sensitivity to the amount of CN in the Clfilms. Their sensitivity is manifested as secondary features in RSoXS profiles that emerge immediately even with 0.5% CN. Then domains continue to grow from ≈100 nm (0.5% CB) to ≈200 nm (with 1% CN) before the NFA crystals eventually grow into tens of micrometer domains with 2% CN. In the F-systems, on the other hand, the secondary features form with relatively higher concentration of CN >1%, where micrometer-scale domains suddenly appear in the 2% CN film. This seems to be dependent on the type of halogenation where CN enables stronger aggregation, phase separation, or intermolecular interaction in the CPDT-4Cl molecules than CPDT-4F. Such a difference could originate from a stronger interaction of the Cl-NFA with CN due to the matched halogens as compared with the unmatched F-NFA. Further investigation remains required to examine the thermodynamic effects of CN on the different types of halogenations.

At the optimal processing conditions of this study, 1% CN, the F-blend has domains with size ≈50 nm, whereas Cl-blends are composed of multilength domains ≈25 and ≈200 nm. Although the primary small domains are beneficial for exciton dissociation, having relatively large features in the Cl-blends may aid as continuous pathways that facilitate charge transport to the electrodes. In comparison, the F-blend with 1% CN consists of only small domains which may increase the possibility of having isolated domains that act as traps. If that scenario is true, then it might be the explanation to why trap-assisted charge recombination was higher in the F-blend than Cl-blend.

The charge recombination was examined previously via measurements of  $V_{\rm oc}$  as a function of incident light intensity. [25] We cannot rule out the possibility of coexistence of impure domains in the F-blend with 1% CN for two reasons. First, quantitative examination of domain purity in that BHJ sample via STXM was limited due to domain size being below the resolution limits of the technique. [38] Second, although the Clblend with 1% CN contains 100% pure domains via RSoXS and STXM, also the RSoXS TSI of the 1% CN F-blend point toward domains with high purity, none of that is enough to quantitatively measure domain purity in the F-blend without absolute scattering intensities. Thus, it is possible that the relatively higher rate of trap-assisted recombination in the F-blend with 1% CN may be due to some percolation via domain mixing.

To examine potential structure-property relations in the investigated BHJ systems, FF and  $J_{\rm sc}$  are plotted in Figure 9a,b as functions of normalized TSI. [36] The data of the 2% CN blends are not presented in Figure 9, but the results—as mentioned above-confirm high domain purity regardless of the relatively lower normalized TSI. That drop in TSI for the 2% CN blends is attributed to reduction in volume fraction of the small domains of NFAs as they migrate into largely crystalized domains. Clear correlations can be seen in Figure 9 where both device parameters, FF and  $J_{\rm sc}$ , increase monotonically with domain purity of the primary features. Those primary features, i.e., small domains, are size-compatible with the standard exciton diffusion length (≈10 nm) in OSCs. Linear correlation between domain purity and FF is often found in OSC, [36] where domain purity suppresses charge recombination. In the investigated F-blends, the device FF improved by about 60% up to the optimum CN concentration. Interestingly, the average domain purity as measured by the normalized TSI is about 60% higher over the same series. The Cl-blend processed from CB has FF = 47% that improves to 66% with 1% CN. We also find direct correlation between  $J_{sc}$  and domain purity, which is usually known for reducing charge recombination.[36]

Another important morphological aspect is crystallinity, which improves with amount of the plasticizer additive in the investigated films, potentially aiding charge transport across the active layers. [32] Positive correlations between FF and coherence length of small-molecules has been established in many NFA systems. [33] We did not see any obvious trends in the  $D_{\rm coh}$  values of  $\pi$ - $\pi$  stacking with solvent additive. Therefore, we plotted FF and  $J_{\rm sc}$  in Figure 9c,d as functions of the diffraction peak intensity of  $\pi$ - $\pi$  stacking of the NFAs, the latter is often related to the relative degree of crystallinity (rDoC). [32] We

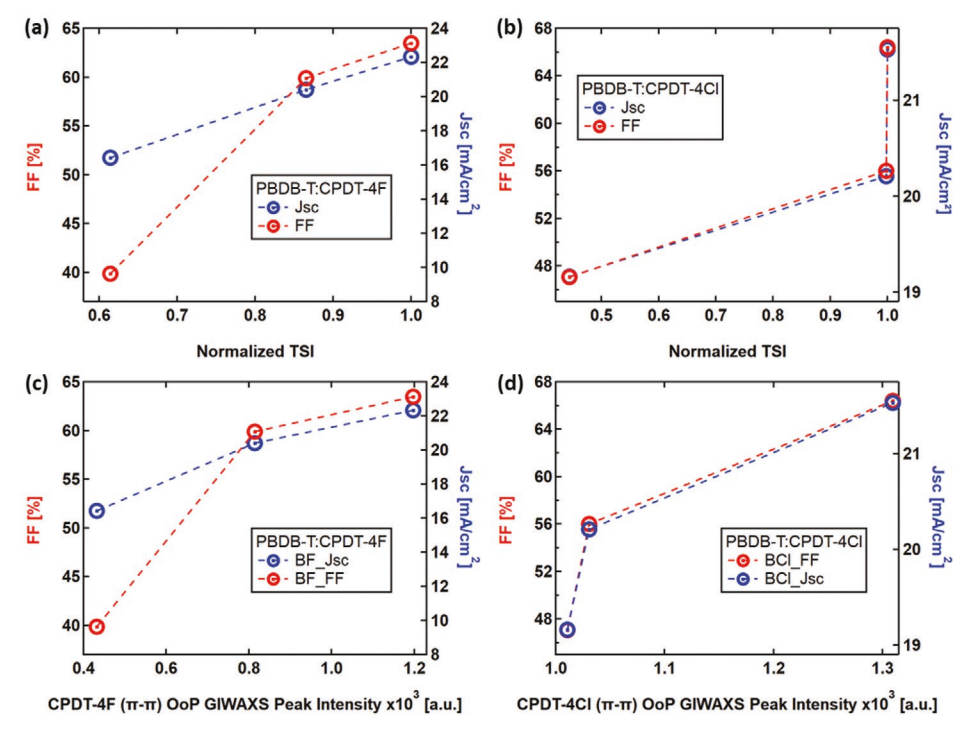


Figure 9. FF and  $J_{sc}$  plotted as functions of normalized TSI for the a) PBDB-T:CPDT-4F blends and b) Cl-blends. FF (red circles) plotted on the left y-axis and  $J_{sc}$  (blue circles) on the right y-axis. FF and  $J_{sc}$  plotted as functions of GIWAXS peak intensity of the NFA  $\pi$ – $\pi$  stacking for the c) F-blends and d) Cl-blends. Note that the presented results here are for blends with 0, 0.5, and 1 vol% CN.

similarly find a monotonic relationship between the face-on  $\pi-\pi$  stacking intensity of the NFAs and the device parameters; FF and  $J_{\rm sc}$ . However, 2% CN leads to over-crystallization, high domain purity, and oversized domains that likely result in poor efficiency of exciton dissociation and thus low  $J_{\rm sc}$ .  $^{[15]}$  On the other hand,  $V_{\rm oc}$  constantly decreases as the concentration of solvent additive increases which can be attributed to the improved crystallinity.  $^{[48]}$  Increased electron delocalization due to crystallinity is known for lowering the acceptor's lowest unoccupied molecular orbital (LUMO) energy level which reduces  $V_{\rm oc}$ . At the same time, crystallinity decreases charge recombination which increases  $V_{\rm oc}$ . It appears that the former effect dominates the latter in the investigated NFA systems. This behavior is commonly observed in many OSCs systems with processing additives.  $^{[49-51]}$ 

Importantly, the oversensitivity of device performance and morphology of NFA systems to the amount of processing additive is similar to the detrimental behavior seen in small-molecule:fullerene systems.<sup>[20]</sup> The findings of this work would suggest the significant reduction in device performance of those CPDT-based OSCs that we have observed previously,<sup>[25]</sup> even with 0.1% CN above optimum, can be attributed to potentially undesirable crystallization and strong phase separation. This suggests that CN probably is not a compatible solvent additive for large scale fabrication of NFA OSCs as extreme precision is required to avoid any excess amount of additive that could result nucleation of large-scale crystallization that ruins the panel. It is worth mentioning that the solvent additive used here, CN, is a commonly used plasticizer to optimize device performance in many of the state-of-the-art NFA

systems such as PM6:Y6. [3,52] Although device performance and perhaps morphology of PM6:Y6 system seem less sensitive to amount of processing additive around optimal conditions, [3,18] extra residuals of solvent additive result in drastic evolution in molecular packing, leading to significant reduction in device performance. [53,54] The extreme device-performance sensitivity of PM6:Y6 OSCs to concentrations of CN was found in films with thickness (400 nm) that is better suitable for industrialscale production. Specifically, the optimal amount of CN (1.5%) yields PCE = 14.4%, while 1.8% of CN gives only 8.6%. [53] Initial microscopic results of ongoing work, provided in Figure S29 (Supporting Information), manifest the morphological sensitivity of PM6:Y6 blends to excessive amounts of CN. However, thorough morphological investigations of the sensitivity of this novel system to concentrations of processing additive need further exploration.

Routes to overcome such an issue include introducing alternative additives, [55] binary solvent additives, [56] nonvolatile solid additives, and third components as in ternary OSCs. [15,57] For example, we have previously substituted the halogen element Cl in the CN molecule with F or Br to mitigate phase separation in PM6:Y6 OSCs and achieved 17.5% PCE. [18] Thus, modifying molecular structure to resist runaway crystallization may be one route to make OSCs more robust. Other work focuses on substituting CN with a halogen-free additive that actually shows comparable effects on optimizing efficiencies in PM6:Y6 OSCs. [58] It is noticeable in the latter study that the device performance is quite tolerant to the amount of additive beyond optimum. This result is consistent with ours that similar halogens on the additive and NFA may increase the propensity to crystallize. Despite





achieve successful fabrication of NFA OSCs. We also examined the impacts of the type of halogenation of NFAs (fluorination vs chlorination) on meso-structures and found that the Cl-molecules show a higher rate of aggregation. Results of this work give insights onto the effects of halogenation and solvent additive on morphology and device performance of synthetically simple, near infrared CPDT-NFA based OSCs.

the successful lab endeavors to optimize device performance in NFA OSCs, scaling up device fabrication with processing additives imposes many challenges. For example, optimization of the rheological properties of BHJ inks and extreme precision to avoid undesirable solvent residuals are required when processing large-area devices with plasticizers. [59] Additionally, any excessive residuals of solvent additives that lead to undesirable morphologies such as strong aggregation result in film hardness that is incompatible with roll-to-roll fabrication. [60] Overall, the long-term stability of devices processed with additives like CN remains questionable. [15]

# There are some possible alternative strategies for industrial printing of NFA OSCs. That includes manipulating BHJ ink concentrations to optimize device performance, [60] exploring eco-friendly single solvent compatibilities with BHJ materials, [61] and re-engineering of NFA molecular structures for better morphological outcomes.<sup>[62]</sup> Successful approaches to avoid issues related to solvent additives are even encouraging to target additive-free fabrication methods. For example, Jeong et al. have successfully blade-cast PTB7-th:EH-IDTBR OSCs with device area of 85 cm $^2$ and PCE > 8% by simply controlling the ink concentrations. That showcases an additive-free and temperature-independent printing method that can be potentially implemented in large scale to prevent undesirable effects of those processing treatments on film structures.[60] Other exciting work by Dong et al. of synthesizing a Y6 derivative (named DTY6) with longer alkyl chains resulted in a good solubility in non-halogen (o-xylene) solvent and suppressed excessive aggregations compared to Y6. They found that PM6:DTY6 OSCs, processed from a single non-halogen solvent, outperform the record-efficiency PM6:Y6 devices. That also allowed for fabrication of blade-cast devices with active areas of $18\ cm^2$ and certified PCE of 13.98%.[62] Although we have only focused on CN in this study, the findings encourage devoting more attention to explore alternative additive-free strategies of largescale production of NFA OSCs to control the sensitivity to processing additives.

# 4. Conclusion

In this study, a characterization of device performance and morphology of PBDB-T:non-fullerene OSCs was conducted to examine their sensitivity to the processing additive. CN was used as a plasticizer additive to optimize device performance. We find the device performance to be very sensitive to the amount of additive where PCE was almost doubled up to the optimum concentration, 1% CN. Here, domain purity and crystallinity strongly correlate with device FF and  $I_{sc}$  up to optimal conditions. However, any additional increments in the concentration of the additive, beyond optimum, lead to a drastic fall off in device performance. Excessive phase separation and overcrystallization occur in the blends with 2% CN, leading to large NFA crystals which we interpret as the main cause to poor performance. The over sensitivity of device performance and morphology to the processing additive in the examined NFA OSCs is remarkable. This seemingly common issue among many small-molecule systems stresses the importance of careful selections of solvent additive or even additive-free methods to

# 5. Experimental Section

Device Fabrication: The device structures were ITO/PEDOT:PSS/ active layer/Phen-NaDPO/Ag. Organic solar cell devices were fabricated using ITO-coated glass substrates (15  $\Omega$  sq<sup>-1</sup>),which were cleaned with detergent water, deionized water, acetone, and isopropyl alcohol in an ultrasonic bath sequentially for 20 min, and further treated with UV exposure for 30 min in a UV-ozone chamber. A thin layer (≈30 nm) of PEDOT:PSS (Bayer Baytron 4083) was first spincoated on the precleaned ITO-coated glass substrates at 4000 rpm and baked at 160 °C for 15 min under ambient conditions. The substrates were then transferred into a nitrogen-filled glovebox. Subsequently, the precursors of the photoactive layer were stirred overnight at 80 °C before spinning. The optimized overall concentrations were 22 and 20 mg mL<sup>-1</sup> chlorobenzene solution with feed ratio of 1:1.2 (w/w) and 1:1 (w/w) for PBDB-T: acceptors, respectively. Solvent additive, 1-CN, was used to improve the intermixing of the electron donor and acceptor phases. The spin speed was 2000 rpm, and the corresponding thickness was around ≈100 nm. Then Phen-NaDPO as the electron transporting layer was spin-coated on the active layer by 2000 rpm from isopropyl alcohol solution. At the final stage, the substrates were pumped down in high vacuum at a pressure of  $3 \times 10^{-4}$  Pa, and Ag layer (100 nm) was thermally evaporated onto the active layer. Shadow masks were used to define the OSC active area (0.11 cm<sup>2</sup>) of the devices.

Device Testing: J–V Curves and External Quantum Efficiency: The current density–voltage (J–V) characteristics of unencapsulated photovoltaic devices were measured under  $\rm N_2$  using a Keithley 2400 source meter. A 300 W xenon arc solar simulator with an AM 1.5 global filter operated at 100 mW cm<sup>-2</sup> was used to simulate the AM 1.5G solar irradiation. The illumination intensity was corrected by using a silicon photodiode with a protective KG5 filter calibrated by the Nationals Renewable Energy Laboratory (NREL). The external quantum efficiency (EQE) was performed using certified IPCE equipment (Zolix Instruments, Inc., Solar Cell Scan 100). The average parameters were calculated from ten independent cells.

X-Ray Measurements: Synchrotron X-ray diffraction, microscopy, spectroscopy, and scattering were used to investigate the nanomorphology of the active layers in those NFA OSCs. The X-ray measurements (NEXAFS/STXM, RSoXS, GIWAXS) were conducted at the Advanced Light Source (ALS) at Berkeley National Lab in CA at 5.3.2, [63] 11.0.1.2, [40] and 7.3.3 [30] beamlines, respectively. The fabrication of the examined films was the same as the J-V devices which is similar to the previously published batch of OSC devices.  $^{\left[ 25\right] }$  GIWAXS data were conducted with hard X-ray (energy = 10 keV) at an angle of incidence = 0.2°, which is higher than the critical angle of the Si substrate. Samples were cast on PEDOT:PSS layer on Si substrates. RSoXS data were conducted at X-ray energies 270 and 285.2 eV. Thin films—from the same substrates as the GIWAXS films—were floated off in deionized water onto low stress  $Si_3N_4$  membrane with size = 2 mm<sup>2</sup> and thickness = 100 nm. NEXAFS absorbance spectra were collected at the same spot of each film as where the RSoXS data were taken to determine the exact thickness of the scattering part of each film. Then RSoXS data were normalized to thickness film. STXM images were acquired at resonant energies of the polymer and small molecule materials as indicated in graph captions and legends in main text and the Supporting Information. The imaging energies were selected based on the NEXAFS spectra of the neat materials (see Figure S8, Supporting Information).





STXM and NEXAFS were combined to extract quantitative, chemical maps of composition. The STXM and NEXAFS samples were floated off in deionized water onto TEM grids from the same substrates used for GIWAXS and RSoXS.

Atomic Force Microscopy and Scanning Electron Microscopy: The AFM and SEM samples were cleaved from the same substrates that were prepped for the X-ray measurements. The film roughness was probed via AFM (Dimension Icon, Bruker) with SCANASYST-AIR silicon tip on nitride lever (70 kHz, 0.4 N m<sup>-1</sup>). The film topology and cross section of the 2% CN blend films were acquired via SEM (QUANTA FEG250, FEI) with the electron gun at 30 kV or SEM Tescan Vega3. The samples were sputter coated with gold for better surface conductivity.

Transmission Electron Microscopy: Samples were cast on PEDOT:PSS/Si substrates and then floated in deionized water onto TEM grids for TEM measurements. TEM images were acquired in bright-field mode via FEI Technai G2 20 Twin (Thermo Fisher, Waltham MA) with a 200 kV LaB6 electron source and FEI Eagle 4k CCD camera detector or via a Talos F200S.

Statistical Analysis: The sample size of J-V measurements is ten independent devices (n = 10 cells). The presented parameters are the mean ± standard deviation. The AFM data were processed using Gwyddion 2.60 software (n = 1). The root-mean-square (RMS) roughness was extracted for the distribution of surface height over the probed film area of each film. The probed film areas are: (2  $\mu m \times 2 \mu m$ ) for pure materials, (15  $\mu m \times$  15  $\mu m$ ) for PBDB-T:CPDT-4F blend with 2% CN, (20  $\mu m \times$  20  $\mu m$ ) for the PBDB-T:CPDT-4Cl blend with 2% CN, and  $(5 \,\mu\text{m} \times 5 \,\mu\text{m})$  the rest of the blend films. Custom software based in Igor Pro was used to process and analyze all X-ray data for RSoXS, STXM/ NEXAFS, and GIWAXS. Sample size for all those X-ray measurements is n = 1. For the GIWAXS measurements, (n = 1), 2D scans collected via CCD camera were reduced into 1D profiles via custom and Nika software. [64] The reduced 1D profiles were then normalized to film thickness, sample length, and X-ray exposure time. Peaks of interest were Gaussian fitted, with fit parameters [peak position, peak height (intensity), and full width at half maximum (FWHM)]. Fitting results of peak intensity were presented with error bars that were extracted from peak fitting. Other fitting results such as FWHM of specific GIWAXS peaks were used in Scherrer analysis to calculate coherence lengths. RSoXS data were processed like GIWAXS, but with a custom software based on Igor Pro. That takes into account other important experimental parameters such as background readings of the CCD camera and X-ray intensity of direct beam at a given scattering energy. NEXAFS spectra analysis for composition and optical constants calculations was conducted using custom Igor Pro based codes. Details of spectra peak fitting, residuals, chi-squared value, and origin of uncertainties can be found in a previously published procedure. [35] Also, a custom software was used to convert STXM data into quantitative composition maps, details of the analysis of composition maps can be found in a previous procedure.[34]

## **Supporting Information**

Supporting Information is available from the Wiley Online Library or from the author.

# Acknowledgements

This work was funded mainly by the U.S. National Science Foundation DMR Electronic and Photonics Program under Grant No. 1905790. This grant supported O.A. V.M. and D.G. were supported by the U.S. Department of Energy Early Career Research Program under Grant No. DE-SC0017923. This research used resources of the Advanced Light Source, which is a DOE Office of Science User facility under Contract No. DE-AC02-05CH11231. Also, this research used the resources of the Franceschi Microscopy & Imaging Center at Washington State University.

### **Conflict of Interest**

The authors declare no conflict of interest.

## **Data Availability Statement**

The data that support the findings of this study are available from the corresponding author upon reasonable request.

# **Keywords**

nanomorphology sensitivity, near-infrared absorbance, non-fullerene small molecules, organic solar cells, resonant X-ray scattering

Received: April 21, 2022 Published online:

- Q. Liu, Y. Jiang, K. Jin, J. Qin, J. Xu, W. Li, J. Xiong, J. Liu, Z. Xiao, K. Sun, S. Yang, X. Zhang, L. Ding, Sci. Bull. 2020, 65, 272.
- [2] C. Li, J. Zhou, J. Song, J. Xu, H. Zhang, X. Zhang, J. Guo, L. Zhu, D. Wei, G. Han, J. Min, Y. Zhang, Z. Xie, Y. Yi, H. Yan, F. Gao, F. Liu, Y. Sun, *Nat. Energy* **2021**, *6*, 605.
- [3] J. Yuan, Y. Zhang, L. Zhou, G. Zhang, H.-L. Yip, T.-K. Lau, X. Lu, C. Zhu, H. Peng, P. A. Johnson, M. Leclerc, Y. Cao, J. Ulanski, Y. Li, Y. Zou, Joule 2019, 3, 1140.
- [4] S. Li, W. Liu, C.-Z. Li, M. Shi, H. Chen, Small 2017, 13, 1701120.
- [5] S. M. McAfee, J. M. Topple, I. G. Hill, G. C. Welch, J. Mater. Chem. A 2015, 3, 16393.
- [6] A. F. Eftaiha, J.-P. Sun, I. G. Hill, G. C. Welch, J. Mater. Chem. A 2014, 2, 1201.
- [7] Y. Lin, X. Zhan, Mater. Horiz. 2014, 1, 470.
- [8] G. Chai, Y. Chang, Z. Peng, Y. Jia, X. Zou, D. Yu, H. Yu, Y. Chen, P. C. Y. Chow, K. S. Wong, J. Zhang, H. Ade, L. Yang, C. Zhan, *Nano Energy* 2020, 76, 105087.
- [9] Y. Wang, Y. Zhang, N. Qiu, H. Feng, H. Gao, B. Kan, Y. Ma, C. Li, X. Wan, Y. Chen, Adv. Energy Mater. 2018, 8, 1702870.
- [10] Z. Liu, X. Zhang, P. Li, X. Gao, Sol. Energy 2018, 174, 171.
- [11] R. Ma, G. Li, D. Li, T. Liu, Z. Luo, G. Zhang, M. Zhang, Z. Wang, S. Luo, T. Yang, F. Liu, H. Yan, B. Tang, Sol. RRL 2020, 4, 2000250.
- [12] R. Geng, X. Song, H. Feng, J. Yu, M. Zhang, N. Gasparini, Z. Zhang, F. Liu, D. Baran, W. Tang, ACS Energy Lett. 2019, 4, 763.
- [13] S. Furukawa, T. Yasuda, J. Mater. Chem. A 2019, 7, 14806.
- [14] H.-C. Liao, C.-C. Ho, C.-Y. Chang, M.-H. Jao, S. B. Darling, W.-F. Su, Mater. Today 2013, 16, 326.
- [15] C. McDowell, M. Abdelsamie, M. F. Toney, G. C. Bazan, Adv. Mater. 2018, 30, 1707114.
- [16] R. Datt, Suman, A. B., A. Siddiqui, R. Sharma, V. Gupta, S. Yoo, S. Kumar, S. P. Singh, Sci. Rep. 2019, 9, 8529.
- [17] J. J. van Franeker, M. Turbiez, W. Li, M. M. Wienk, R. A. J. Janssen, Nat. Commun. 2015, 6, 6229.
- [18] J. Lv, H. Tang, J. Huang, C. Yan, K. Liu, Q. Yang, D. Hu, R. Singh, J. Lee, S. Lu, G. Li, Z. Kan, Energy Environ. Sci. 2021, 14, 3044.
- [19] X. Song, N. Gasparini, D. Baran, Adv. Electron. Mater. 2018, 4, 1700358.
- [20] O. Alqahtani, M. Babics, J. Gorenflot, V. Savikhin, T. Ferron, A. H. Balawi, A. Paulke, Z. Kan, M. Pope, A. J. Clulow, J. Wolf, P. L. Burn, I. R. Gentle, D. Neher, M. F. Toney, F. Laquai, P. M. Beaujuge, B. A. Collins, Adv. Energy Mater. 2018, 8, 1702941.
- [21] P. Dhakal, T. Ferron, A. Alotaibi, V. Murcia, O. Alqahtani, B. A. Collins, J. Phys. Chem. Lett. 2021.





- [22] S. Mukherjee, C. M. Proctor, J. R. Tumbleston, G. C. Bazan, T.-Q. Nguyen, H. Ade, Adv. Mater. 2015, 27, 1105.
- [23] S. Engmann, F. A. Bokel, A. A. Herzing, H. W. Ro, C. Girotto, B. Caputo, C. V. Hoven, E. Schaible, A. Hexemer, D. M. DeLongchamp, L. J. Richter, J. Mater. Chem. A 2015, 3, 8764.
- [24] S. Xie, J. Wang, R. Wang, D. Zhang, H. Zhou, Y. Zhang, D. Zhou, Chin. Chem. Lett. 2019, 30, 217.
- [25] K. Wang, J. Lv, T. Duan, Z. Li, Q. Yang, J. Fu, W. Meng, T. Xu, Z. Xiao, Z. Kan, K. Sun, S. Lu, ACS Appl. Mater. Interfaces 2019, 11, 6717.
- [26] W. Shockley, H. J. Queisser, 11.
- [27] J. Lee, S.-J. Ko, M. Seifrid, H. Lee, B. R. Luginbuhl, A. Karki, M. Ford, K. Rosenthal, K. Cho, T.-Q. Nguyen, G. C. Bazan, Adv. Energy Mater. 2018, 8, 1801212.
- [28] S. Li, L. Zhan, W. Zhao, S. Zhang, B. Ali, Z. Fu, T.-K. Lau, X. Lu, M. Shi, C.-Z. Li, J. Hou, H. Chen, J. Mater. Chem. A 2018, 6, 12132.
- [29] S. Li, L. Zhan, F. Liu, J. Ren, M. Shi, C.-Z. Li, T. P. Russell, H. Chen, Adv. Mater. 2018, 30, 1705208.
- [30] A. Hexemer, W. Bras, J. Glossinger, E. Schaible, E. Gann, R. Kirian, A. MacDowell, M. Church, B. Rude, H. Padmore, J. Phys. Conf. Ser. 2010, 247, 012007.
- [31] S. Engmann, J. Mater. Chem. A 2015, 8.
- [32] T. P. Chaney, A. J. Levin, S. A. Schneider, M. F. Toney, *Mater. Horiz.* 2021, 10.1039.D1MH01219C.
- [33] H. Hu, K. Jiang, P. C. Y. Chow, L. Ye, G. Zhang, Z. Li, J. H. Carpenter, H. Ade, H. Yan, Adv. Energy Mater. 2018, 8, 1701674.
- [34] B. A. Collins, Z. Li, J. R. Tumbleston, E. Gann, C. R. McNeill, H. Ade, Adv. Energy Mater. 2013, 3, 65.
- [35] B. A. Collins, H. Ade, J. Electron Spectrosc. Relat. Phenom. 2012, 185, 119.
- [36] X. Jiao, L. Ye, H. Ade, Adv. Energy Mater. 2017, 7, 1700084.
- [37] O. Alqahtani, S. M. Hosseini, T. Ferron, V. Murcia, T. McAfee, K. Vixie, F. Huang, A. Armin, S. Shoaee, B. A. Collins, ACS Appl. Mater. Interfaces 2021, 13, 56394.
- [38] M. A. Marcus, D. A. Shapiro, Y.-S. Yu, Microsc. Microanal. 2021, 27, 1448.
- [39] L. J. Richter, D. M. DeLongchamp, F. A. Bokel, S. Engmann, K. W. Chou, A. Amassian, E. Schaible, A. Hexemer, Adv. Energy Mater. 2015, 5, 1400975.
- [40] E. Gann, A. T. Young, B. A. Collins, H. Yan, J. Nasiatka, H. A. Padmore, H. Ade, A. Hexemer, C. Wang, Rev. Sci. Instrum. 2012, 83, 045110.
- [41] B. A. Collins, E. Gann, J. Polym. Sci. 2022, 60, 1199.
- [42] F. Cser, J. Appl. Polym. Sci. 2001, 80, 2300.
- [43] Y. Qin, Y. Xu, Z. Peng, J. Hou, H. Ade, Adv. Funct. Mater. 2020, 30, 2005011.

- [44] I. Angunawela, L. Ye, H. Bin, Z.-G. Zhang, A. Gadisa, Y. Li, H. Ade, Mater. Chem. Front. 2019, 3, 137.
- [45] L. Zhang, H. Zhao, B. Lin, J. Yuan, X. Xu, J. Wu, K. Zhou, X. Guo, M. Zhang, W. Ma, J. Mater. Chem. A 2019, 7, 22265.
- [46] J. R. Tumbleston, B. A. Collins, L. Yang, A. C. Stuart, E. Gann, W. Ma, W. You, H. Ade, Nat. Photonics 2014, 8, 385.
- [47] S. Mukherjee, X. Jiao, H. Ade, Adv. Energy Mater. 2016, 6, 1600699.
- [48] K. Vandewal, K. Tvingstedt, A. Gadisa, O. Inganäs, J. V. Manca, Phys. Rev. B 2010, 81, 125204.
- [49] Z. Zheng, E. He, J. Wang, Z. Qin, T. Niu, F. Guo, S. Gao, Z. Ma, L. Zhao, X. Lu, Q. Xue, Y. Cao, G. T. Mola, Y. Zhang, J. Mater. Chem. A 2021, 9, 26105.
- [50] Q. Zhao, H. Lai, H. Chen, H. Li, F. He, J. Mater. Chem. A 2021, 9, 1119
- [51] B. Fan, D. Zhang, M. Li, W. Zhong, Z. Zeng, L. Ying, F. Huang, Y. Cao, Sci. China Chem. 2019, 62, 746.
- [52] H. Song, D. Hu, J. Lv, S. Lu, C. Haiyan, Z. Kan, Adv. Sci. 2022, 9, 2105575.
- [53] S. M. Hosseini, N. Tokmoldin, Y. W. Lee, Y. Zou, H. Y. Woo, D. Neher, S. Shoaee, Sol. RRL 2020, 4, 2000498.
- [54] S. Karuthedath, Y. Firdaus, A. D. Scaccabarozzi, M. I. Nugraha, S. Alam, T. D. Anthopoulos, F. Laquai, Small Struct. 2022, 3, 2100199.
- [55] M. Li, J. Liu, X. Cao, K. Zhou, Q. Zhao, X. Yu, R. Xing, Y. Han, Phys. Chem. Chem. Phys. 2014, 16, 26917.
- [56] W.-Z. Fo, G. Y. Xu, H.-J. Dong, L.-N. Liu, Y. W. Li, L. Ding, Macromol. Chem. Phys. 2021, 222, 2100062.
- [57] S. Dong, K. Zhang, T. Jia, W. Zhong, X. Wang, F. Huang, Y. Cao, *EcoMat* 2019, 1, e12006.
- [58] L. Ye, Y. Xiong, M. Zhang, X. Guo, H. Guan, Y. Zou, H. Ade, *Nano Energy* 2020, 77, 105310.
- [59] P. Xue, P. Cheng, R. P. S. Han, X. Zhan, Mater. Horiz. 2022, 9, 194.
- [60] S. Jeong, B. Park, S. Hong, S. Kim, J. Kim, S. Kwon, J.-H. Lee, M. S. Lee, J. C. Park, H. Kang, K. Lee, ACS Appl. Mater. Interfaces 2020, 12, 41877.
- [61] L. Ye, Y. Xiong, Q. Zhang, S. Li, C. Wang, Z. Jiang, J. Hou, W. You, H. Ade, Adv. Mater. 2018, 30, 1705485.
- [62] S. Dong, T. Jia, K. Zhang, J. Jing, F. Huang, Joule 2020, 4, 2004.
- [63] A. L. D. Kilcoyne, T. Tyliszczak, W. F. Steele, S. Fakra, P. Hitchcock, K. Franck, E. Anderson, B. Harteneck, E. G. Rightor, G. E. Mitchell, A. P. Hitchcock, L. Yang, T. Warwick, H. Ade, J. Synchrotron Radiat. 2003, 10, 125.
- [64] J. Ilavsky, J. Appl. Crystallogr. 2012, 45, 324.